CHAPTER 3

Hyperspectral case study 2. Captains Flat (NSW) - Acid Mine Drainage pollution

3.1 Introduction

3.1.1 Location

The Captains Flat mine workings are situated on the Molonglo River, approximately 50 kilometres southeast of Canberra in NSW (Figure 3.1). The location of the mine is latitude 35.5833S, longitude 149.4333E and 889m above sea level. Although the tailings of this mine were rehabilitated in the mid 1970's, acid metal-rich waters draining from the mine and tailings dumps continue to pollute the river destroying the ecology and contributing to some pollution of Lake Burley Griffin in Canberra (Dames & Moore, 1993). Particular mineral precipitates are an indicator of the source and magnitude of the pollution and this study is an attempt to use hyperspectral remote-sensing to locate these minerals.

3.1.2. Study Site

The orebody at Captains Flat consists of massive and disseminated sulphide and occurs in a north-south trending belt of Silurian shale and volcanics (Glasson and Paine, 1965; Oldershaw, 1965). The orebody is developed stratigraphically above a rhyolite crystal tuff and is overlain by a coarse dacitic crystal tuff (Glasson and Paine, 1965). The sulphides consist mainly of pyrite followed by sphalerite, galena, chalcopyrite, arsenopyrite, tennantite, and minor gold.

The Captains Flat mining operations commenced in 1882 and continued periodically until 1962. The workings were underground with surface ore processing, smelting and waste storage facilities producing zinc, pyrite, lead, copper, silver and gold. During mining, mine and mill water containing zinc was regularly discharged into the Molonglo River and there were three incidents when tailings and slime dams collapsed

depositing high concentrations of copper, iron and zinc, into the flooded Molonglo River. This led to the destruction of vegetation along the Molonglo River (Hogg, 1990). Aquatic fauna and flora has degraded as a consequence of continued acid mine drainage (AMD) pollution along the Molonglo River between Captains Flat and Canberra. This has included the loss of macro-invertebrates and fish (Weatherley, 1967; Norris, 1986). Remedial works were completed in 1976 in order to reduce the risk of increased pollution. Rehabilitation involved reshaping the tailings dumps and capping them with compacted clay, shale and soil, and sowing grasses and legumes (Craze, 1977). The position of the rehabilitated dumps are shown in Figure 3.2.

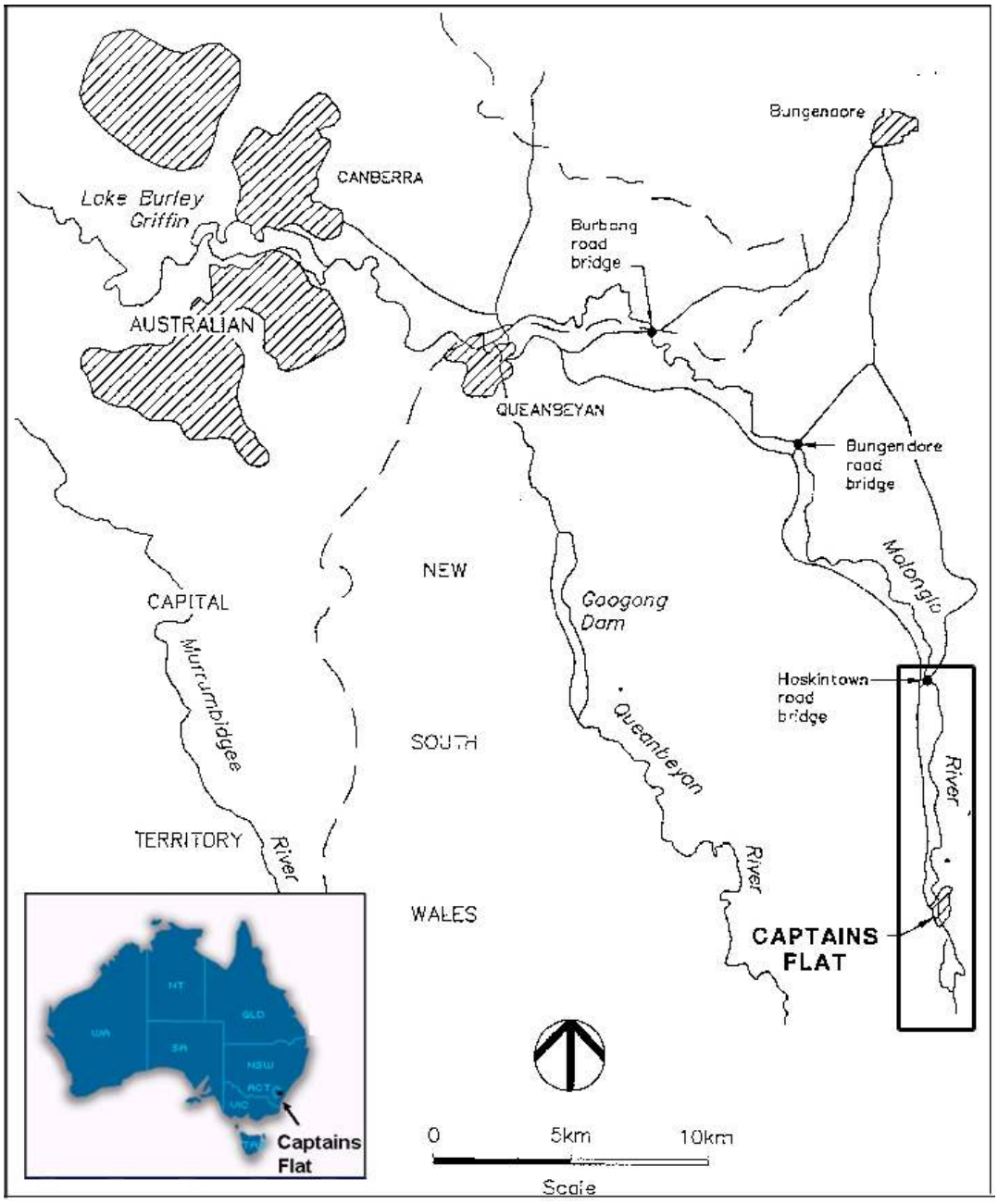

Figure 3.1. Location of Captains Flat (From Dames & Moore, 1993) and the HyMap survey area.

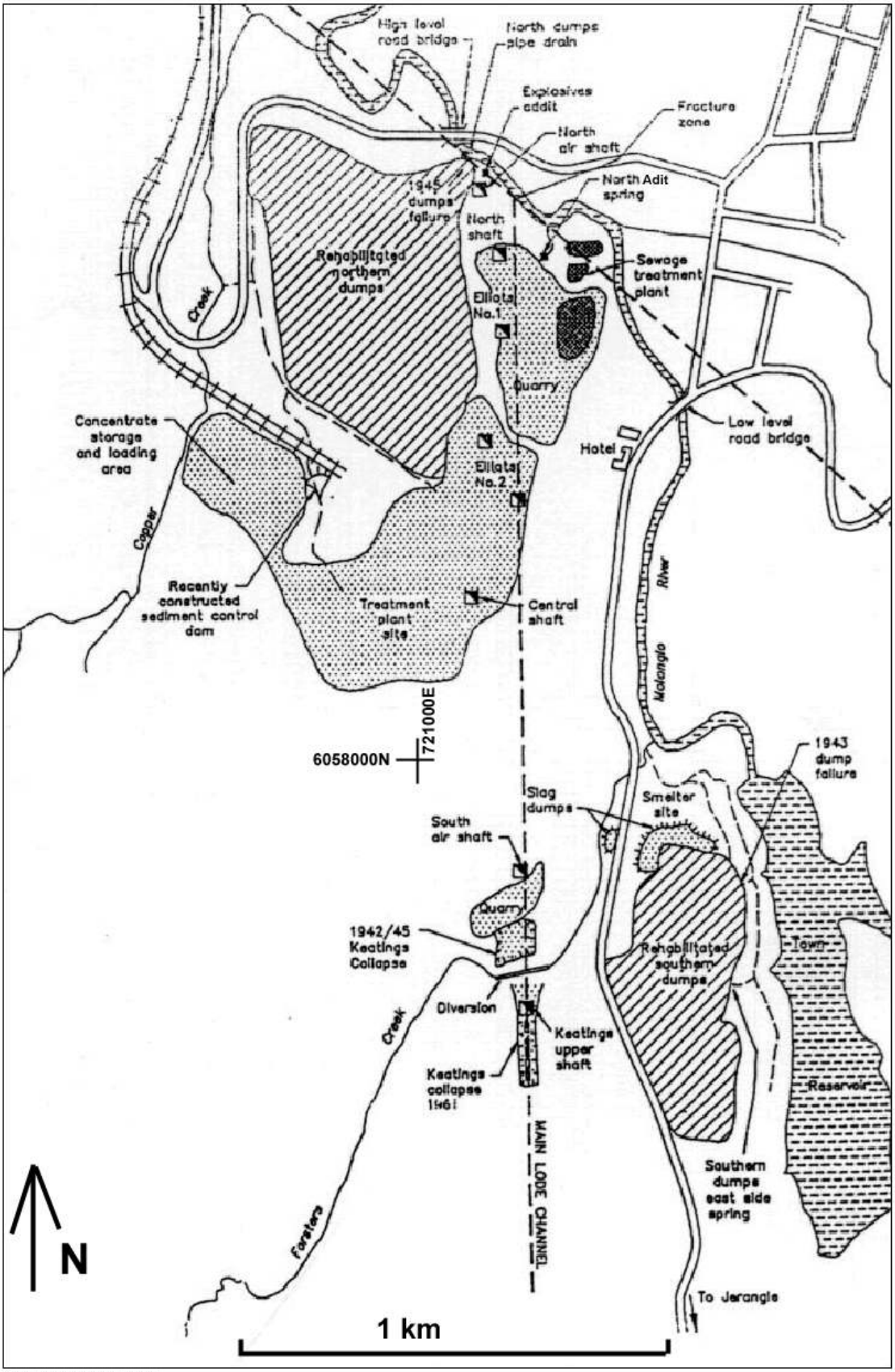

Figure 3.2. Captains Flat mine site. From Dames and Moore, (1993).

Ten years after the rehabilitation work, it was found that levels of metals, in water and sediments, including zinc and cadmium (exceeding safe drinking levels) as well as biota degradation, were similar to pre-rehabilitation levels (Norris, 1986). Moreover, Jacobson and Sparksman (1988) found that zinc levels in Molonglo River water were similar to 1973 levels for up to 10km downstream that high zinc concentrations were found in sediments 40 km downstream. Metals, particularly zinc in water and sediments, remain a source of pollution to Lake Burley Griffin in Canberra (Dames & Moore, 1993).

The township of Captains Flat is located on the eastern side of the Molonglo River in close proximity to the mine site and dumps. Although the Captains Flat workings were successfully rehabilitated in terms of major objectives, the site clearly remains disturbed and degraded. Thus while the remediation appears to have reduced the pollution, significant seepages are still produced by the high-pressure head of groundwater in the mine (Jacobson and Sparksman, 1988) and probably also in the dumps. Some of the seepage areas are shown in Figure 3.3. At the northern end of the quarry (see Fig. 3.2) is a large discharge of mine water seepage called the North Adit Spring. This spring is considered the primary source of pollution during dry periods and discharges within metres of the Molonglo River (see photo Figure 3.4). Other discharges occur close by, namely the Explosives Adit, Fracture zone and Pipe Drain (emanating from the Northern Dumps). Seepages from the southern dumps also contribute to the pollution, some of it directly into the town reservoir (see Figure 3.3, bottom-right). The pH of the water can be as low as 2.5 and consistently below 3 from the North Adit spring (Hogg, 1990).

The aereal extent and depth of contaminated sediments in the Molonglo River has never been accurately defined and there is uncertainty in defining the contribution that re-mobilization of contaminants from sediments makes to the overall pollution of the river (Dames and Moore, 1993). Thus although it can be argued that remediation has reduced the heavy metal loads in water and sediments lower in the catchment, pollution in the upper Molonglo River is still significant (Hogg, 1990). Given that it is difficult to stop the flow of acid mine drainage so close to the river, current thinking is that chemical or wetland treatment of the seepage waters would significantly improve the ecology of the river (Dames and Moore, 1993).

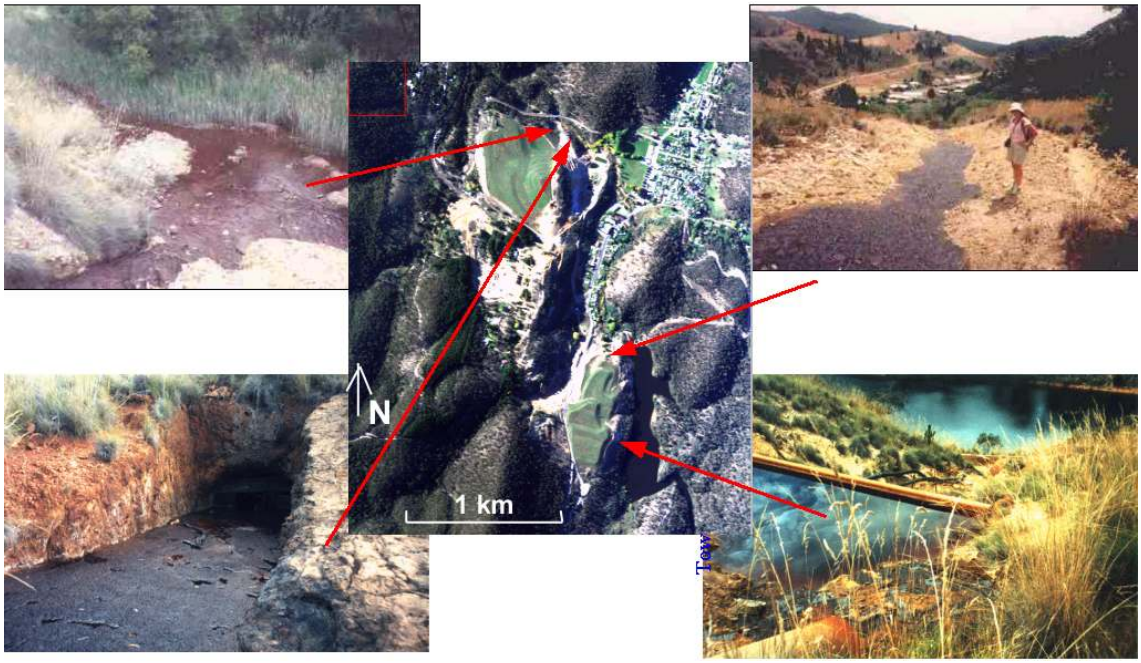

Figure 3.3 Photos of seepage areas around the mine area. The central image is a visible band combination from the HyMap data. The central image can be located by reference to the features in Figure 3.2.

The aereal extent and depth of contaminated sediments in the Molonglo River has never been accurately defined and there is uncertainty in defining the contribution that re-mobilization of contaminants from sediments makes to the overall pollution of the river (Dames and Moore, 1993). Thus although it can be argued that remediation has reduced the heavy metal loads in water and sediments lower in the catchment, pollution in the upper Molonglo River is still significant (Hogg, 1990). Given that it is difficult to stop the flow of acid mine drainage so close to the river, current thinking is that chemical or wetland treatment of the seepage waters would significantly improve the ecology of the river (Dames and Moore, 1993).

Figure 3.4. Seepage of acid mine waters at North adit spring. Brown areas in the water are amorphous Fe-minerals (see text).

3.1.3 Acid mine drainage and mineral associations

Minerals that precipitate from acid waters draining from base metal mine workings are useful targets for remote sensing since they indicate the source, extent and conditions of environmental pollution. In this context, the precipitates of interest are iron oxyhydroxides, oxyhyroxysulfates and sulfates (Schwertmann and Fitzpatrick, 1992). These minerals are often very fine grained and can be intermixed at a variety of scales. A variety of chemical conditions influence the types of minerals that are precipitated including the presence of ions , pH and Eh (Fitzpatrick and Self, 1997). During the weathering of sulphides, most commonly pyrite, in the mine rocks and spoils, Fe(II) ions are oxidised to fe(III) and then hydrolysed to form Fe(III) oxides and oxyhydroxides (Schwertmann and Fitzpatrick, 1992). Water draining mine sequences often contain dissolved Fe(II) and when strongly acid, Fe(III) ions. Once formed, Fe(III) oxides are generally stable in an aerobic environment. At low pH (<3), microorganisms assist the oxidation and formation of Fe(III) minerals. A paragenetic relationship exists between the common Fe(III) bearing minerals in these environments: jarosite, schwertmannite, ferrihydrite and goethite (Bigham et al, 1996). In very acid mine waters (pH < 2.5) jarosite will precipitate and with increasing pH the dominant Fe

phases will be schwertmannite and ferrihydrite respectively. All three minerals become metastable with respect to goethite when pH exceeds ~ 2, i.e. over much of the range associated with mine drainage waters. Precipitate minerals and their formulas are given in Table 3.1 and each of these are described in detail below.

Table 3.1 AMD minerals and their formulas.

Ferrihydrite	$Fe_5HO_8.4H_2O$
Schwertmannite	$Fe_8O_8(OH)_6SO_4$
Goethite	alpha FeOOH
Lepidocrocite	gamma FeOOH
Hematite	alpha Fe_2O_3
Jarosite	$KFe_3(OH)_6(SO_4)_2$
Natrojarosite	$NaFe_3(SO_4)2(OH)_6$
Hydronium jarosite	$(K,H_30)Fe_3(S0_4)_2(OH)_6$
Gypsum	$CaSO_4.2H_2O$
Copiapite	$Fe^{+2}(Fe^{+3})_4(SO_4)_6(OH)_2 \bullet 20H_2O$

3.1.3.1 Ferrihydrite

Ferrihydrite is probably the most important mineral precipitate in an acid mine drainage environment because of it's capacity for adsorption of heavy metals (Schwertmann and Fitzpatrick, 1992; Jambor and Dutrizac, 1998) due to the large surface area. It forms by the rapid oxidation and hydrolysis of containing-waters suddenly appearing at the surface. Ferrihydrite is a reddish-brown, poorly crystalline mineral - the formula and structure of which are not incontrovertibly resolved (Jambor and Dutrizac, 1998). Where newly formed, ferrihydrite consists of gel-like deposits that after drying forms yellow-brown ochres (Chukhrov et al, 1974). Formation of ferrihydrite rather than goethite from drainage waters is favoured by higher rates of oxidation, concentration of nuclei and higher sulfate to Fe ratios (Brady et al, 1986). The pH range for stability is from about 5 to 9 and it can display a range in structure that gives XRD patterns varying from 6-line (best crystalline) to 2-line (worst crystalline) (Eggleton and Fitzpatrick, 1988). Very fine grained (amorphous) ferrihydrite is prepared in the laboratory by the

rapid oxidation of Fe(II) solutions, or by the rapid neutralisation of Fe(III) solutions. More crystalline forms can form by the hydrolysis of Fe(III) solutions at elevated temperatures and low pH. Being unstable, it eventually transforms to goethite or hematite via a dissolution-recrystallization process although it is unclear how long this takes under normal environmental conditions. Ferrihydrite is often observed in recent sediments associated with lakes, rivers and groundwater (Jambor and Dutrizac, 1998; Fitzpatrick et al, 1997).

3.1.3.2 Jarosite

Jarosite forms under very acidic conditions (pH < 2.5) in the presence of sulfate ions (Schwertmann and Fitzpatrick, 1992). There is a solid solution series between jarosite (K-rich), natrojarosite (Na-rich), hydronium jarosite ($H_3$0-form) and NH4 jarosite. Although there is a preference for the K-form, natrojarosite has also been observed in acid-mine drainage environments (Brady et al, 1986). Jarosite forms yellow deposits in mine drainage or mine spoils and it may be stable up to a pH of about 4 (Van Breemen, 1988). If the pH increases or the sulfate decreases, jarosite becomes unstable and the complete hydrolysis of Fe^{3+} ions often results in the formation of ferrihydrite or goethite.

3.1.3.3 Schwertmannite

Schwertmannite is a common mine drainage material (Fitzpatrick and Self, 1997; Bigham et al, 1996; Swayze et al, 1996; Schwertmann et al, 1995) that forms in acid conditions (pH 2.8 –4.5) and high sulfate concentrations. Like ferrihydrite, it is a poorly crystalline, yellowish brown mineral with a fibrous morphology. It forms in place of ferrihydrite where the waters are acid. For solutions at pH 4.5-6.5, precipitates may be a mixture of schwertmannite, ferrihydrite and goethite (Bigham et al, 1996). Schwertmannite in water may transform to goethite within days of precipitation although complete transformation may take over 500 days (Bigham et al, 1996).

3.1.3.4 Goethite

Although present, often in abundance, in acid mine drainage from the breakdown of sulfides, goethite and hematite are also commonly found as weathering products of silicate minerals in rocks and soils. In AMD, goethite, yellow-brown in colour, forms where oxidation is slow enough to allow crystal growth from solution and it may also form by transformation from ferrihydrite (Schwertmann, 1985) and jarosite (Schwertmann and Fitzpatrick, 1992). Goethite is stable above pH = 4 (van Breeman, 1988). In the transformation from ferrihydrite, goethite forms from solution, i.e., after dissolution of ferrihydrite (Schwertmann, 1988). This is in preference to hematite where the activity of water is higher and temperatures are lower (see hematite below).

3.1.3.5 Lepidocrocite

Lepidocrocite is typically bright orange and often forms associations with its polymorph goethite. It is often found in soils as a result of reduction of Fe-oxides soils due to O_2 deficiency and subsequent re-oxidation (Schwertmann, 1988). It has also been observed in AMD materials (Jambor and Dutrizac, 1998). Lower carbonate ions in solution favor lepidocrocite over goethite formation.

3.1.3.6 Hematite

Hematite forms by dehydration and structural rearrangement of ferrihydrite which is considered a necessary precursor. It is red-coloured and factors that induce hematite formation in place of goethite are low water activity, higher temperature, low humidity, high rate of Fe release from rocks and low organic matter concentrations. Hematite is often the dominant Fe-oxide in well-drained, dryer soils (Schwertmann, 1988). Experimental evidence suggests that at neutral pH, hematite will form from ferrihydrite whereas goethite develops at acid and alkaline conditions (Schwertmann and Murad, 1983).

3.1.3.7 Gypsum

A hydrated calcium sulfate, gypsum is stable in moderately acid conditions, pH 4-6.5, but not in reducing conditions (Brookins, 1988). It is generally formed by evaporation

of waters containing calcium sulfate, but it also formed by the action of sulfuric acid solution on calcium bearing minerals (Deer et al, 1992) Gypsum is rarely described in acid-mine drainage studies although experimental studies show that in the presence of $CaCl_2$ solutions, large amounts of gypsum will form with increasing pyrite oxidation (Ludwig et al, 1999).

3.1.3.8 Other sulfates

Other soluble metal sulfate salts such as melanterite, chalcanthite, coquimbite, rhomboclase, voltaite, copiapite, and halotrichite have been identified in acid mine drainage, and some of these are forming from negative-pH mine waters (Nordstrom and Alpers, 1999). Soluble Fe-oxyhydroxysulphates such as copiapite are a temporary store of contaminant metals, but are dissolved during periods of high rainfall or flooding, releasing contaminants to the aqueous system.

3.1.4 Known Spectral features of AMD materials.

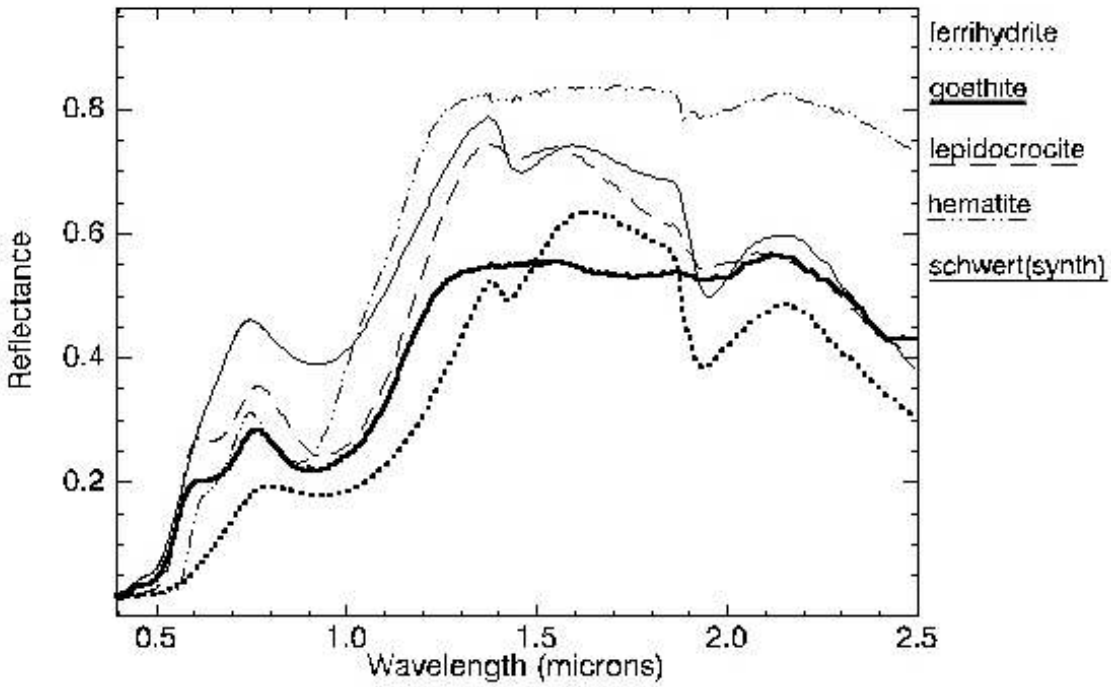

Figure 3.5. VNIR and SWIR spectra for iron minerals associated with acid mine drainage. All spectra are from the USGS spectral library apart from schwertmannite (Gregg Swayze, pers. com.)

The iron minerals in Figure 3.5 all show a low broad absorption in the visible (0.4-0.7 μm) due to electron transfer between ferric and oxygen ions (Hunt and Ashley, 1979). Crystal field transitions are responsible for the spectral variations between 0.45 and 0.95 μm. These vary according to the crystal structure of the different minerals. In general, the position of the band near 0.85 μm is an indicator of the presence of hematite. The broad water features at 1.4 and 1.9 μm in the ferrihydrite spectrum indicate water molecules occupying unordered sites (Hunt, 1977).

In AMD, unoxidized pyrite is sometimes present but lacks spectral features (Figure 3.6). Sulfates formed as part of the weathering process, however, have significantly different spectra. Jarosite has a characteristic sharp absorption at 0.43 μm and a broad absorption at 0.9 μm due to ferric ion transition (Hunt and Ashley, 1979). Both jarosite and gypsum also have features due to OH vibrational overtones in the 2.2 – 2.3 μm range. Gypsum also shows water absorption features near 0.99, 1.2, 1.45, 1.495, 1.539, 1.75 and 1.948 μm making this mineral spectrally distinctive. Copiapite shows ferric iron features in the VNIR but also low reflectance in the SWIR due to a high water content.

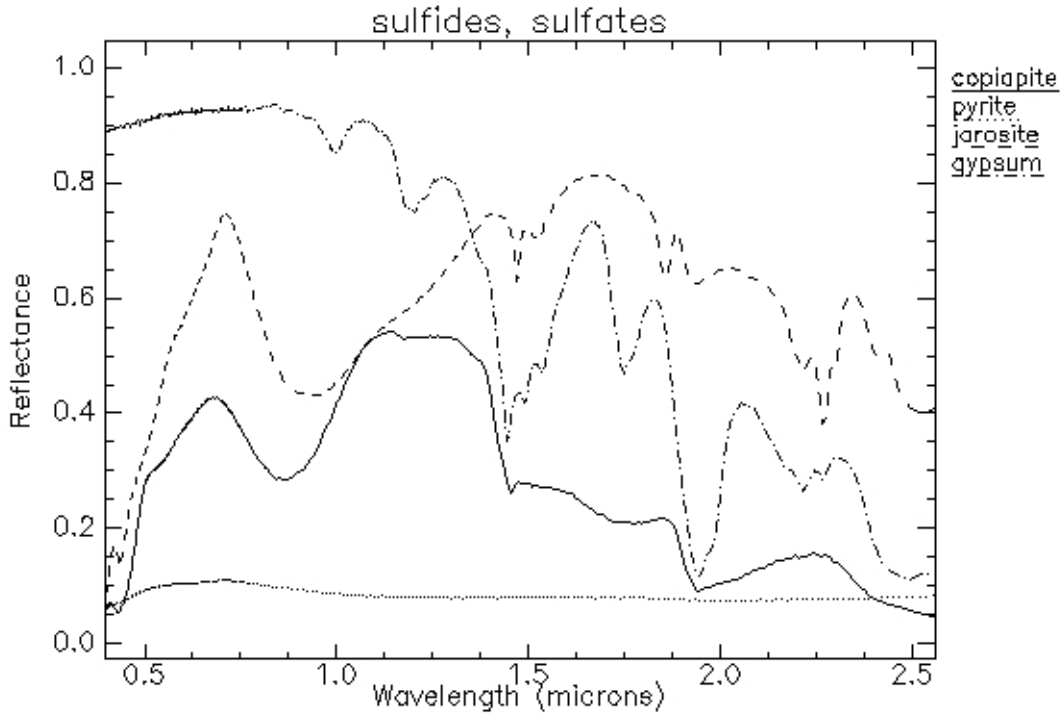

Figure 3.6 VNIR and SWIR spectra for sulfur minerals associated with acid mine drainage. All spectra are from the USGS spectral library.

3.1.5 Previous remote sensing work on acid-mine drainage

Airborne imaging spectroscopy is established as a tool for mine waste evaluation although mainly in the USA (Dalton et al, 2000; Swayze et al, 1996; Swayze et al, 2000). Most of this work has been carried out by the USGS and employs the AVIRIS hyperspectral instrument to map mine waste materials. Images derived from the data using a band mapping technique known as the "tetracorder" algorithm (Clark et al, 1990b) have been demonstrated to map pyrite- weathering products: jarosite, goethite and hematite (direct spectral detection of pyrite is hampered by its low reflectance level). In particular, jarosite zones are sources of toxic metal mobility and are locations of acid generation. Jarosite may be associated with efflorescent iron-sulfate salts such as melanterite and copiapite (Swayze et al, 2000). These zones are surrounded by less acid goethite-rich areas. Hematite may occur within goethite zones. Swayze et al (2000) recognize ferrihydrite and schwertmannite as mine-waste materials but don't map them since they claim that goethite dominates spectrally. One explanation is that the "tetracorder" algorithm they use cannot discriminate these materials due to its method of analysing feature position and depth. The approach used in their method of separating the spectrum into two regions and analysing them separately may also reduce its effectiveness.

3.1.6 Hyperspectral image acquisition

At the beginning of the project, only one airborne hyperspectral dataset existed at Captains Flat. This was an HyMap 128-band data-set, covering the 0.42 -2.48 μm range (see Appendix 1) and collected over Captains Flat on 16/04/1999 at 5 metre pixel resolution. The full flight strip covers approximately 16 km by 60 m. This data-set had been acquired by Hyvista Corporation as an evaluation exercise for the application of hyperspectral data to monitor acid-mine drainage pollution. One problem with this data was a strong shadow component due to the survey time (3.41 pm) in April with a low solar elevation angle in an area of steep topography. From the survey time, the solar azimuth was calculated to be 300.3 degrees and the solar elevation was 21.4 degrees. The effect of this problem on mineral identification processing, together with a means to correct for these illumination effects, is discussed in section 3.3.1.1.

A second opportunistic acquisition of HyMap was conducted on 31/03/2001 at 3 metre pixel resolution. The acquisition time was 1.30pm and, compared with the first survey, the more northerly solar azimuth (329.4 degrees) and larger solar elevation angle (45.7 degrees) meant that topography effects were much reduced. Also, this time there was an opportunity to lay out homogeneous targets for radiometric calibration. Further details of the second survey and the calibration targets are discussed in Section 3.3.2.

3.2 Field sampling and analysis – results.

Field investigations involved collection of 34 ASD field spectra and 50 Unispec (VNIR) spectra of selected mineral precipitates, rocks, water, vegetation, shade and invariant targets. Samples of acid mine drainage precipitates were collected from known seepage areas - sample locations are shown in Figure A2.1. Further laboratory studies, including XRD analyses, electron microprobe and ASD spectral analyses, were conducted on selected samples to determine mineralogy and verify spectral results.

Table 3.2. Comparison of mineral identifications from XRD and VNIR-SWIR spectra (ASD) for AMD materials in the Captains Flat area. The field locations of these samples are shown in Figure A2.1

Sample No	**XRD ID**	**ASD spectral ID**
CF22	gypsum, goethite, amorphous Fe-mineral	algae water, gypsum(??)
CF29	Gypsum, goethite, natrojarosite, minor quartz	goethite, gypsum(??)
CF33	amorphous Fe-mineral, minor quartz	Fe-mineral, algae, water, gypsum(???)
CF40	gypsum, goethite, minor quartz	goethite, gypsum
CF42	jarosite.hydronian.syn, minor gypsum, quartz and goethite	gypsum, goethite , jarosite(?)
CF44	amorphous Fe-mineral, minor quartz, trace gypsum	Fe-mineral, water
CF47	amorphous Fe-mineral, minor quartz	Fe-mineral, water
CF47.1	amorphous Fe-mineral (schwertmannite),minor	Fe-mineral, water

	quartz, ?	
CF50	gypsum, minor jarosite, minor quartz	gypsum, jarosite
CF50.1	gypsum, minor jarosite, minor quartz	gypsum, jarosite
CF51	natrojarosite, quartz, minor gypsum, minor goethite, minor albite	jarosite
CF61	minor gypsum, goethite and quartz	algae, water
CF84	schwertmannite, quartz, minor goethite	schwertmannite, minor goethite
CF85	schwertmannite, quartz, minor goethite	schwertmannite, minor goethite
CF86	schwertmannite, quartz, minor muscovite	schwertmannite, minor goethite
CF87	schwertmannite, quartz	schwertmannite
CF88	schwertmannite, quartz, muscovite, gypsum	schwertmannite, minor goethite
CF89	quartz, muscovite, ?	muscovite, algae, Fe-mineral

A selection of sample site data for AMD minerals are shown in Table 3.2 and these are discussed in detail in the following sections. ASD spectrometer data were a combination of field (samples CF22–61) and laboratory (samples CF84–89) measurements.

3.2.1 Amorphous Fe-minerals – Schwertmannite, Ferrihydrite

Amorphous (poorly crystalline) Fe-minerals are a common precipitate in the acid waters draining the Captains Flat mine area. The mineral occurs as a fluffy, brownish-yellow material. Figure 3.7 shows ASD field spectra for sites 33, 44 and 47 (all collected from North Adit Spring) and compares these spectra to a laboratory spectrum for ferrihydrite (USGS library) and a spectrum obtained from air-dried material (CF 47). Identification of the mineral species for the Fe-precipitate is difficult using the spectra for acid-mine drainage minerals in Figure 3.5. It is known that amorphous Fe-precipitates in mine drainages are either Schwertmannite or Ferrihydrite or a mixture of these minerals (Bigham et al, 1996) and that the spectra of these minerals are similar (see Figure 3.5).

At Captains Flat, these materials appear to only be present in water. This complicates spectral identification of Schwertmannite and Ferrihydrite since many of the features in the field spectra for CF33, 44 and 47 are water absorptions at 0.97 and 1.158 μm. However, the reflectance peak at 0.74 μm corresponds to the Schwertmannite laboratory spectrum whereas Ferrihydrite has this feature at 0.785 μm.

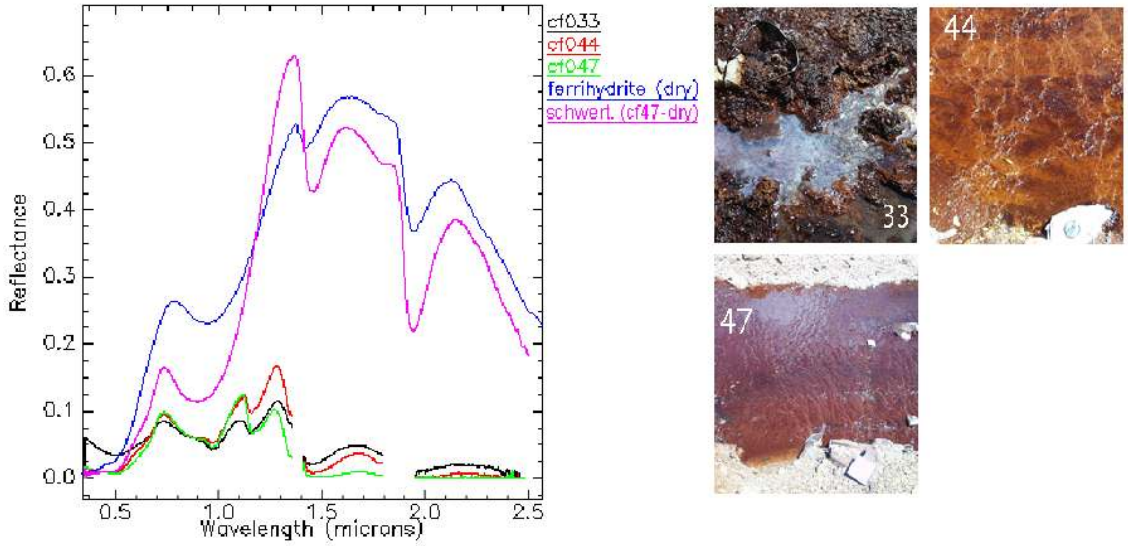

Figure 3.7. Field spectra of amorphous Fe-minerals and accompanying photographs at right. The blue spectral curve for ferrihydrite is from the USGS spectral library.

Figure 3.8 shows an XRD trace for sample CF 47.1; an ocherous, amorphous iron-rich precipitate sampled from the bottom of the stream flowing from the North Adit. Analysis was conducted quickly after collection to minimize mineral transformation due to the unstable nature of the material. This sample was air-dried for 4 hours and measured for an extended time (14 hours) so that a coherent XRD trace could be obtained. Earlier attempts using very moist material and a measurement time of 1.5 hours produced noisy XRD traces (Table 3.2; samples CF33, 44 and 47). These broad features in the XRD trace for CF47.1 (Figure 3.8) indicate poor crystallinity. These broad peaks closely resemble schwertmannite features (Bigham et al, 1996; Childs et al,1998; Bigham et al, 1994). Known schwertmannite peaks are indicated with position on Figure 3.8. Several sharp peaks that are also present are due to the presence of a minor amount of quartz in the sample as judged by the d spacing values (e.g. the peak at a 2θ of 59º). The assymetry of the peak at d=0.256 and the pattern between here and d=0.15 resembles 6-line ferrihydrite (Jambor and Dutrizac, 1998; Eggleton and Fitzpatrick, 1988) although the broad peaks are also consistent with schwertmannite

(Bigham et al, 1994; Childs et al, 1998). The peaks at 0.34 and 0.50 indicate schwertmannite although the exact position of the feature near 0.50 depends on sulfate concentration. A value of d= 0.486 is characteristic of pure schwertmannite (Bigham et al, 1990), i.e. increased sulfate, and given the position at 0.50, it is likely that sample CF47 is a mixture of schwertmannite and ferrihydrite, with the former probably dominating. To resolve this issue, a number of samples were collected from amorphous Fe precipitates at the North Adit spring (CF84 – 88) and from bottom sediment from 10km downstream of the mine (CF 89). These were analysed in the laboratory with (1) Electron microprobe (to find element concentrations) and (2) Visible to SWIR spectroscopy (ASD). The sulphate concentration for the Fe-precipitates (Table 3.3) ranges from 12.89 to 13.46 % which is effectively in the range of pure schwertmannite ; 13-15% SO_3 (Childs et al, 1998, Yu et al, 1999). The electron microprobe results for sample CF89 are interesting in that a high level of toxic Zinc (1.22 % ZnO) is recorded in sediment 10 km downstream from the mine

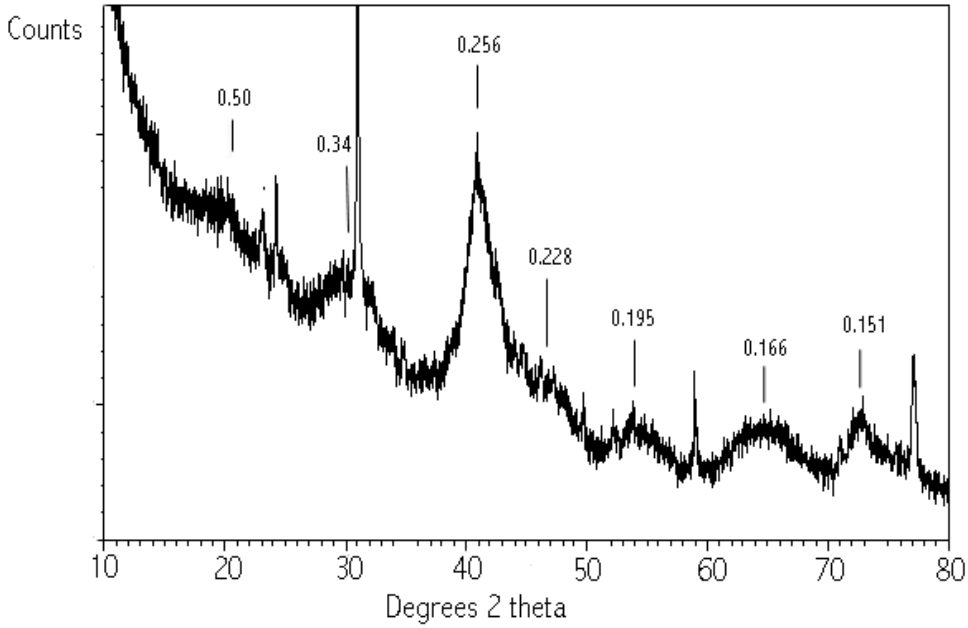

Figure 3.8. XRD trace for sample 47.1, an amorphous Fe-precipitate in water; schwertmannite + ferrihydrite? + quartz. Numbers are d spacings assigned to peaks associated with schwertmannite.

Table 3.3 Electron Microprobe analyses of AMD precipitates

Sample	CF84	CF85	CF86	CF87	CF89
Type	Amorphous Fe-oxide	Amorphous Fe-oxide	Amorphous Fe-oxide	Amorphous Fe-oxide	River sed downstream
SiO2	0.23	0.22	0.35	0.38	74.96
Al_2O_3	-0.01	0.08	0.22	0.07	4.895
FeO	64.19	62.76	56.86	60.59	2.555
MnO	-0.03	-0.14	-0.06	0.08	0.47
MgO	-0.04	0.11	0.06	0.01	0.425
CaO	0.09	0.11	0.02	0.05	0.23
Na_2O	-0.43	-0.45	-0.44	-0.47	0.23
K_2O	0.03	0.14	0.04	0	0.885
SO_3	13.11	13.46	13.29	12.89	0.255
CuO	0.09	0.18	-0.16	-0.06	0.09
ZnO	0.03	-0.13	0.09	-0.17	1.22
Total	77.27	76.36	70.28	73.38	86.22

Similar spectral features were observed for schwertmannite samples CF 84 – 88. Figure 3.9 shows schwertmannite samples CF84 and 87 compared to the library spectra for ferrihydrite (USGS spectral library) and schwertmannite synthesized by Gerry Bigham (Swayze, pers com.). For all the samples identified by XRD and microprobe as schwertmannite (CF84-88), the reflectance peak at 0.74 μm is consistent in position. A small absorption shoulder can be seen at 0.67 μm due to the presence of minor goethite (see Table 3.2) can be seen in the spectrum for CF84. The goethite present in both the XRD sample and the spectral sample may have been produced by transformation of schwertmannite in the approximately 24 hour period between collection and measurements. These spectra may be useful for laboratory identification of schwertmannite but are unlikely to be relevant to field spectra since this mineral is generally mixed with water as shown by the spectrum for CF47.

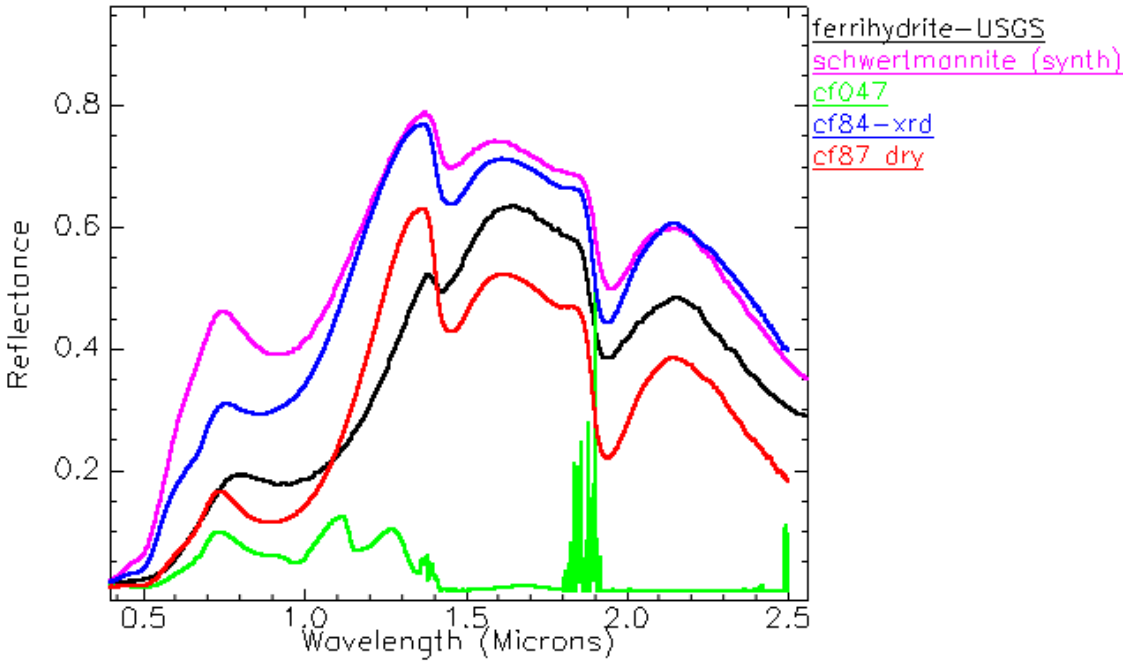

Figure 3.9 VNIR-SWIR spectra, obtained with the ASD spectrometer, for schwertmannite samples at Captains Flat compared with library spectra of amorphous Fe-precipitates. The reflectance peak near 0.74 μm is present in all samples identified as containing schwertmannite.

Sample analysis using XRD, electron microprobe and spectral reflectance has identified much of the amorphous Fe-precipitates in the mine-draining waters as schwertmannite. The presence of this mineral indicates highly acidic and toxic waters (see section 3.1.3.3). The mixed water and schwertmannite signature is therefore a target for hyperspectral remote sensing.

3.2.2 Jarosite, gypsum

In the Captain's Flat area, jarosite forms yellow deposits in mine drainage and exposed mine spoils and it's presence indicates a surface pH less than 4 (Van Breemen, 1988). It is commonly found with gypsum that has formed as a by-product of the oxidation of pyrite. Figure 3.10 shows field spectra of gypsum and jarosite rich samples sites compared with a library spectrum for jarosite. CF50 shows a nearly pure gypsum spectrum (cf. Figure 3.6). Jarosite is present in significant quantities in CF42 and CF51 as determined by XRD analysis (Table 3.2). According to XRD trace analysis, the composition of CF51 was best matched to natrojarosite (see Table 3.1) whereas CF42 matched better to hydronium jarosite. In the spectra for both samples (Figure 3.10), the

high reflectance at 0.71 μm and the broad Fe^{3+} absorption feature centred at 0.9 μm due to jarosite are present. While the narrow 0.44 μm jarosite feature is present clearly in CF51 and CF50, it is only a weak shoulder in CF42. Features due to gypsum are also observed in these spectra, particularly the presence of the diagnostic absorption at 1.75 μm. It appears that an increase in jarosite concentration in CF51 causes the reflectance peak to be at a slightly longer wavelength at 1.34 μm. Mixtures between jarosite and gypsum will produce a reflectance high in this wavelength area and the shape will depend on the relative mix. Gypsum has a decreasing reflectance in this region with increasing wavelength whereas for jarosite, the trend is the reverse.

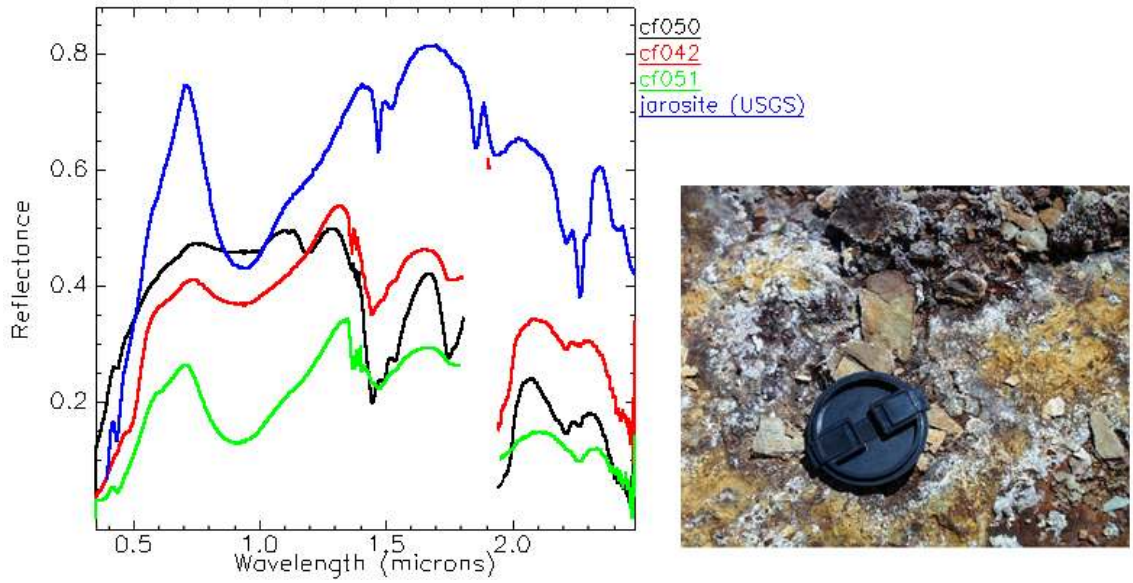

Figure 3.10. Spectra of some samples from Captains Flat containing jarosite (yellow-brown in photograph) and gypsum (white).

3.2.3 Goethite, black algae

Extensive areas of goethite are likely to have formed by transformation of jarosite, given the unstable nature of the latter mineral. CF29 and CF40 are moist areas of slightly exposed gypsum crystals mixed with goethite and their field spectra are shown in Figure 3.11. Jarosite is still present in CF29 and although identified by XRD (see Table 3.2), the only spectral evidence for jarosite in CF29 is a slightly longer wavelength peak at 1.30 μm. Both spectra have features between 0.4 and 0.95 μm that correspond to the lab spectrum of goethite (cf. Figure 3.5) and this is confirmed by

XRD. Again gypsum features are observed with absorption at 1.75 μm and a reflectance high at 1.291 μm.

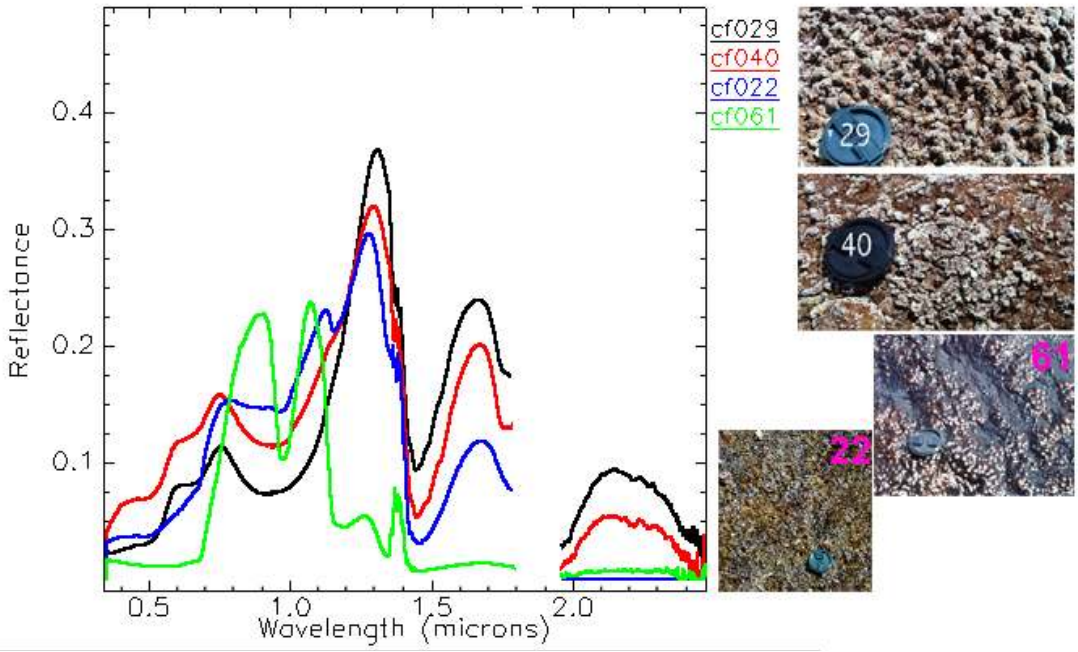

Figure 3.11. ASD spectra of some samples from Captains Flat containing a goethite and gypsum mixture (CF29 and CF40), algae (CF61) and a mix of all of these (CF22).

A common feature in mine drainages is a gelatinous dark coloured algae identified as Chlorophyceae (Green Algae) – Oedogonium (C. Young, pers com). The spectrum for this material (CF61) is shown in Figure 3.11. In the XRD, only small amounts of gypsum, goethite and quartz were found in this sample. The ASD spectrum shows a very dark visible response with almost no green component. A chlorophyll absorption feature or "red edge" is present at 0.67 μm while water absorption features are present at 0.976 μm and 1.156 and the sample absorbs almost totally after about 1.4 μm. CF22 is an area of "crystalline soup" and represents a mixture of all the above materials. Again the water feature at 0.97 μm obscures the position of the ferric iron feature. The reflectance peak at 0.78 μm appears to indicate the presence of ferrihydrite rather than schwertmannite although the XRD analysis indicates only the presence of either.

3.2.4 Materials in water

As mentioned before, the presence of water features in spectra may complicate the detection of materials like schwertmannite or ferrihydrite when they occur in streams. The question is whether there are spectral differences between them and ordinary sediments in shallow water. Figure 3.12 shows a number of spectral of materials under a layer of water.

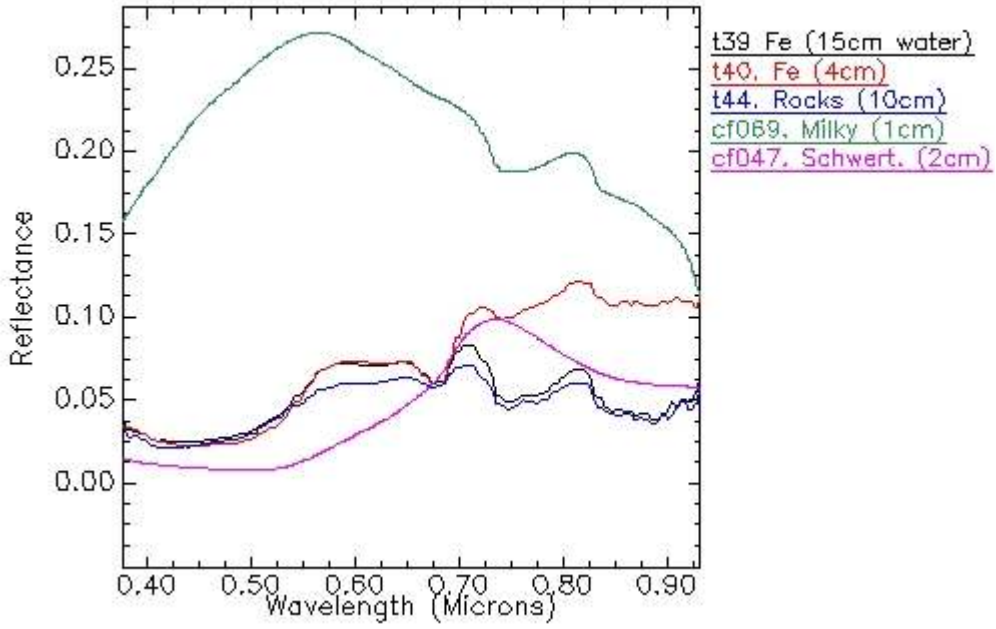

Figure 3.12. Spectra of materials obtained in the field under a layer of river water. Spectra t39, t40 and t44 were measured with the VNIR Unispec spectrometer. CF69 and CF47 were measured with the ASD instrument. Approximate water depths are in brackets.

The Unispec data for t39, t40 and t44 are quite noisy and were all measured about 10km downstream from the mine. Sample t39 and t40 were both from areas where the stream bottom was coated with a layer of sediment, largely mud, organic matter and Fe precipitate, the latter has presumably has come from the mine. These two signatures are similar in the visible to a site (t44) where the stream bottom was rocks with no Fe coating. The increased reflectance of t40 in the NIR is due to shallower water and all three Unispec spectra have a chlorophyll feature due to algae at 0.67 μm. These spectra and the spectrum for a milky white precipitate in 1cm of water have a water absorption at 0.74 μm and a shoulder at 0.83 μm. The white material was not identified by XRD although fine-particle separates have not been analysed as yet. The water features are

not present in the spectrum for AMD material (CF47) apparently due to high reflectance of schwertmannite at 0.74 – 0.78 μm. It appears that fresh mine precipitates close to the source are spectrally distinct in the NIR from normal sediments in water.

3.2.5 Shade effects

Figure 3.13 shows the effects of shielding surfaces from direct sunlight. This simulates the effect to the scanner when pixels are in near shade (i.e. illumination is scattered radiation only). This is a particular problem for the initial Captain's Flat HyMap data set. These experiments were conducted in a clearing in an open woodland area and both the spectralon standard and a piece of pine board were measured in direct sunlight and the total shade of a 2m x 2m sheet of black plastic. We would expect that incoming scattered radiation would be strongest in visible blue light (0.45 μm) and decreasing gradually to longer wavelengths (due to scattering by atmospheric molecules) as is observed for the shaded spectralon in the short wavelengths. However the shade data in Figure 3.13 also show the strong influence of radiation scattering from surrounding vegetation as seen by the weak absorption feature at 0.69 μm. The radiation in the visible (0.4–0.7 μm) is also lower than expected due to the vegetation influence. This demonstrates that correction for shade in image data is not as simple as correcting for the relative proportions of diffuse skylight and direct solar radiation based on an illumination angle.

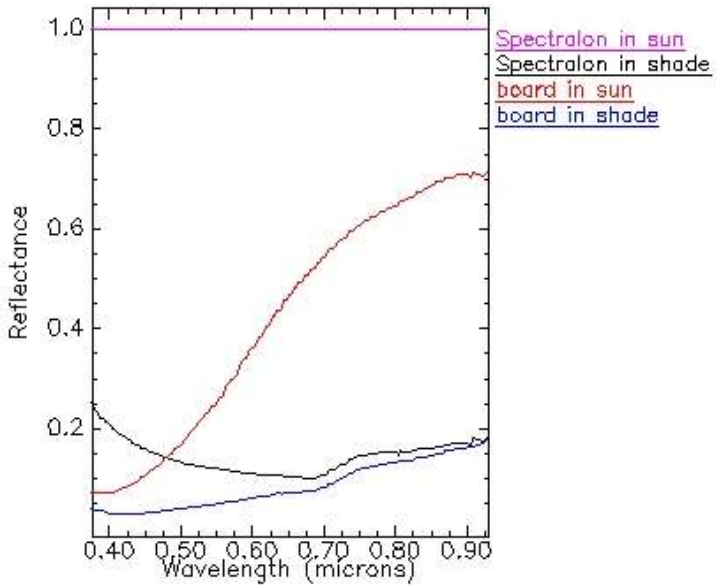

Figure 3.13. Effects of shade. Aerosol scattering increases as wavelength decreases toward 0.4μm as indicated by the rising trend of the spectralon standard in shade.

3.3 Hyperspectral Image analysis

3.3.1 First HyMap survey

As discussed in 3.1.6, two HyMap surveys were flown about 2 years apart. Prior to the second survey, the author believed there might only be one survey data-set to work on. This influenced the processing strategy in that the data needed to be corrected for topographic shading effects and this is discussed below.

3.3.2 Second HyMap survey

When the second survey was flown, only the preliminary analysis had been undertaken on the first survey data. The topographic correction had improved the results but there were still major problems due to the low signal in shade-affected pixels. For analysis of the SWIR bands for minerals like jarosite (see Figure 3.4), the signal was very low and in some areas there was no data. So when the new survey data was clearly superior in terms of radiometric resolution, it was decided to focus on this second data-set for developing surface component themes.

For the new HyMap survey, data were collected in 128 bands from 438 to 2496 nm (see Appendix 1) at an improved 3 metre pixel resolution. Also by this time, Hyvista Corporation, the operator of HyMap had developed a geometric correction based on pitch, roll and heading values acquired on board the aircraft. This was applied to the data using ENVI software geo-correction tools. This time, it was possible to be on the ground during data acquisition and it was decided to lay down some uniform material to act as calibration targets.

3.3.2.1 Calibration targets

The materials used as calibration targets were light-orange and black-plastic building sheets. These were deemed to be uniform in colour and practical in that they could be easily rolled out and maintained. The two coloured plastic sheets were laid out in adjacent 10 metre squares in an open field area on top of the south dump so as to avoid the effects of background reflectance. The location of the sheets is shown on the HyMap image in Figure 3.23. As it was, the sheets were in the field for two weeks as we waited

for suitable weather and logistical conditions to fly the survey. Just prior to the actual survey, they were cleaned and flattened.

Figure 3.23 HyMap band combination equivalent of Landsat TM bands 1,4 and 7 as RGB showing the location of calibration targets on the south dump. The image is 1.5 km across.

3.3.2.2 Calibration to Apparent Reflectance

The HyMap data were initially corrected to reflectance using the HyCorr program (see section 2.2.2). This was done prior to any attempt to calibrate to ground targets since HyCorr uses ATREM to correct for atmospheric gases in each pixel individually. Calibration to ground targets assumes that there are gain and offset effects that influence each pixel in the same way. Therefore any varying effects, e.g. due to atmosphere, should be removed first.

HyCorr reflectance values were averaged for the two pixels at the centre of the ground targets shown in Figure 3.23. These are presented in Figure 3.24 together with ground spectrometer measurements of the two types of plastic sheet. The ASD spectra for the

plastic was provided by Guy Byrne (pers. com.) and were measured outside (under solar illumination) at the CSIRO laboratories. The calibrated airborne data compares very well with the ASD spectra for both bright and dark targets. This indicates that HyCorr is working well in producing realistic reflectance spectra.

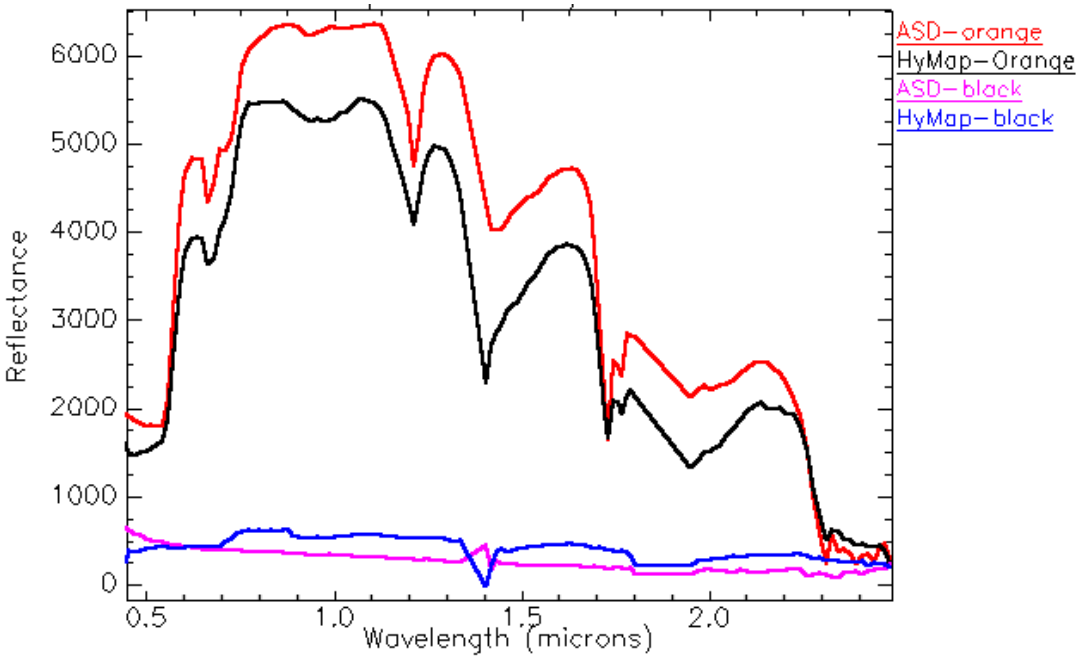

Figure 3.24. HyMap pixel reflectance for orange and black plastic ground targets compared with Fieldspec ASD spectra of the plastic. ASD measurements from Byrne (pers. com.) – CSIRO Land and Water

The ASD curve for the orange plastic (red in Figure 3.24) is noisy in the very low reflectance area at wavelengths greater than 2.27 μm suggesting this material is unsuitable for calibration of these wavelengths. It was important to determine whether the target reflectance information could be used to improve the reflectance calibration or whether the ATREM/EFFORT procedure (HyCorr) was adequate as Figure 3.24 suggests.

3.3.2.3 Reflectance Calibration Using Ground Targets.

The spectra in Figure 3.24 were used to calculate a gain and offset for each band that would convert the HyMap apparent reflectance to the ground spectrometer spectra of the plastic targets. These gain and offset values are shown in Figure 3.25 and were then applied in a linear correction to all pixels to produce a new reflectance data-set.

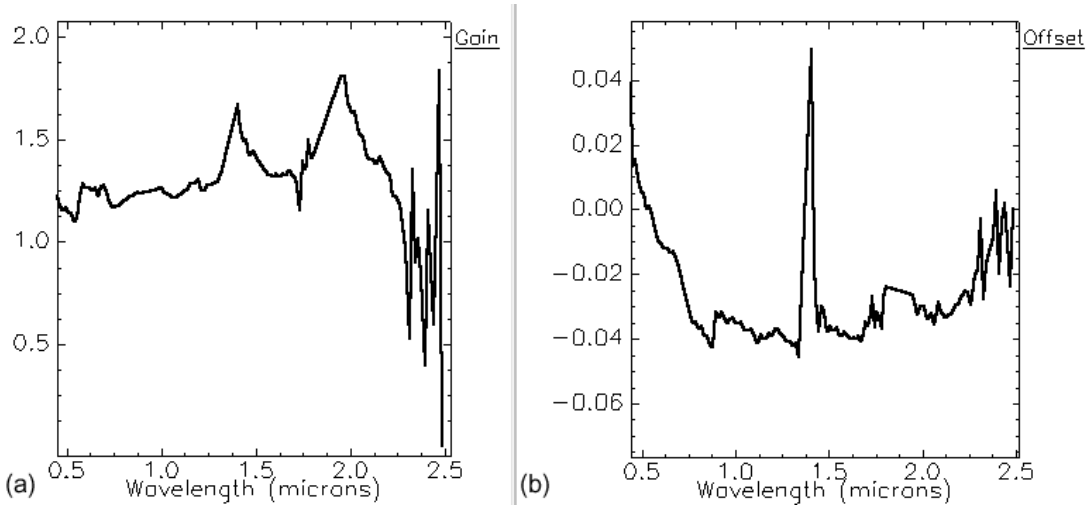

Figure 3.25. (a) Gain and (b) offset values for each band that would convert the HyMap apparent reflectance of calibration targets to the ground spectra.

The gain values are generally greater than 1 due to the ASD measurement of the reflectance of the orange plastic being higher than the airborne HyMap signature (see Figure 3.24). The lower HyMap reflectance could be partly due to the influence of background reflectance, most of which would be from darker vegetation and this is supported by the presence, in the gain values, of inverted vegetation features at 0.54 μm and 0.68 μm. The gain spectrum is very noisy in the 2.25 – 2.5 μm region as a result of the noise in the ASD. The offset spectrum shows an increase towards short visible wavelengths, suggesting that there has been an over-correction for atmospheric scattering in the visible wavelengths by the ATREM routine. There appears to be a similar effect masked partly by noise in the SWIR end of the spectrum although the cause is unclear. Similar effects were also observed in the Pilbara HyMap data (see section 2.5.1). Of greater concern is a significant step in the offset data is observed at 0.877 μm. This highlights a problem in the HyMap data due to a mis-match of radiance data between detectors.

3.3.2.4 Detector mis-match problems in HyMap data and corrections

The detector mis-match between the VNIR and NIR HyMap modules was discovered by the author and in conjunction with Hyvista Corporation, it was found that the mis-match was due to an error in the processing software designed to match the detectors (P. Cocks, pers. com.). This error has now been corrected but had resulted in the

distribution of lesser quality HyMap data from at least March, 2001 to September, 2001. In some pixels the problem creates an artificial feature (see Figure 3.26) that could severely affect the data-analysis.

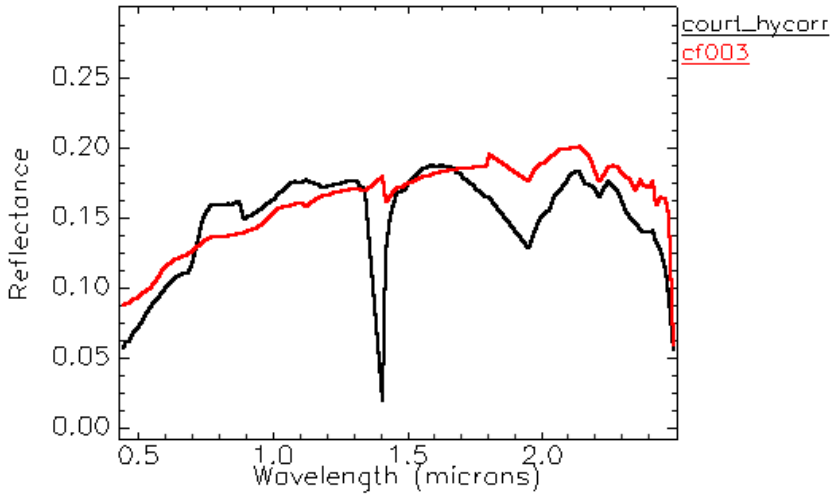

Figure 3.26. Signatures of the ashphalt basketball court from HyCorr corrected HyMap data and FieldSpec ASD (cf003). Note the detector mis-match feature at 0.877 µm.

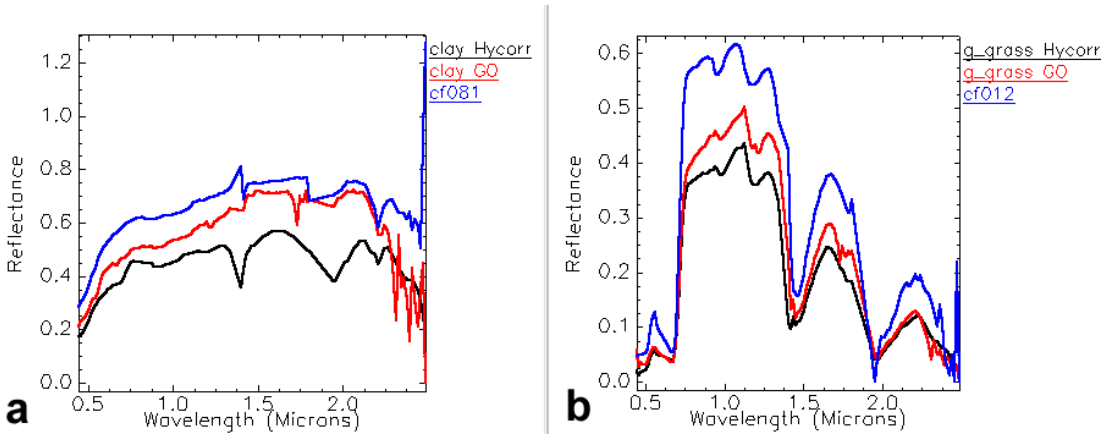

Figure 3.27. Comparison of reflectance corrections; HyCorr (black) and target Gain and Offset (red) calibrations, versus field spectra (blue) for (a) a bare clay area and (b) the green grass of the town oval.

After discovering the detector mis-match, the radiance data were corrected by using a gain factor that forced the overlap band (0.874 µm, see Appendix1) from the NIR module to match the VNIR module. The HyCorr atmospheric program was then re-run and again gain and offsets were found using the ground calibration targets. Figure 3.27 shows the results of the gain and offset correction for (a) an exposed clay-rich road turning area just south of the south tailings dump and (b) an area of green grass on an

oval in the town. The effects of the noise of the calibration target spectra in the SWIR are obvious in the clay spectrum (red in Figure 3.27a) and a sharp feature from the orange plastic spectrum at about 1.73 μm has been introduced. Clearly the presence of sharp features and low reflectance in the SWIR makes the orange plastic unsuitable as a calibration target for the whole spectrum. In the vegetation spectra (Figure 3.27b) the visible spectrum has a better shape although the high NIR reflectance has been dampened.

The gain and offset correction may have slightly improved the VNIR, but in general the reflectance calibration using the ground targets was not successful. This was largely due the use of inappropriate materials, i.e. the low SWIR reflectance and the presence of sharp absorptions in the orange plastic. Also there were background reflectance effects on the targets in the image data. Unfortunately, ideal natural or artificial homogeneous and invariant targets that lacked spectral features could not be found in the Captains Flat scene. Nevertheless, the use of ground targets of known reflectance provided evidence that the HyCorr reflectance correction was adequate (see Figure 3.24).

3.3.2.5 HyMap mapping of surface AMD components

Two main processing strategies were tested for the processing of the HyMap (Data-set 2) into mineral abundance maps: unmixing using image end-members and, unmixing using reference laboratory and field spectra as end-members. Image end-members often work better (Kruse, pers. com.) because they are more closely aligned with the data cloud. However there is a problem in that pure pixels don't really exist so that unmixing results do not target real components. Moreover, in the Captains Flat (Data-set 2) scene, many of the purest pixels found by PPI technique (see section 2.2.4) are man-made objects such as buildings and roofs. Materials such as schwertmannite and jarosite were not found with this method since they occupy small areas and are generally sub-pixel in extent.

For the image end-member approach, a pixel signature for wet schwertmannite (Figure 3.28a) was located in the North Spring adit area, where all the analyzed schwertmannite samples were collected. For jarosite and goethite, image end-members were selected from the highest abundance results obtained from the MTMF method (see section 2.6)

using USGS spectra for these minerals as end-members. This means of finding image end-members assumes that the laboratory end-members can be used to obtain realistic unmixing results at least in the high abundance values. The same method was use to collect the hematite image end-member although constrained in area to the hematite-rich zone (verified by laboratory ASD spectrometry) that was used for concentrate storage and loading (see Figure 3.2). The spectra for image end-members and laboratory/field end- members of the target materials is shown in Figure 3.28.

For the image end-members (Figure 3.28), the jarosite, goethite and hematite spectra are mixtures with clay or mica shown by a strong 2.2 μm feature and look to be also mixed with each other. These three spectra all resemble felsic volcanic rock-type signatures with their varying concentrations of the minerals generally controlled by surface weathering effects. The schwertmannite spectrum (Figure 3.28a) looks more pure (see Figure 3.5) but still appears to be mixed with surrounding material. These spectra really emphasise the difficulty of finding genuinely pure pixels for AMD materials.

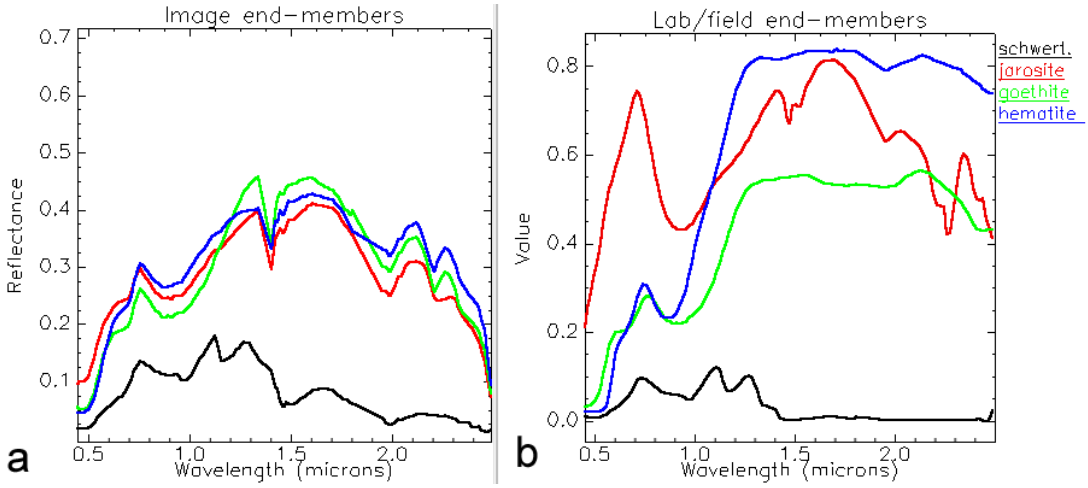

Figure 3.28 (a) Image end-members versus (b) laboratory/ field end-members for AMD target materials. Apart from schwertmannite, the spectra in (b) are from the USGS spectral library.

The MTMF procedure was used to test both image and reference end-members (shown in Figure 3.28) using three spectral ranges; VNIR (0.453 – 1.311 μm), SWIR (2.007 – 2.409 μm) and a combination of both. The Minimum Noise Fraction (MNF) rotation (Green et al, 1988) was first used to reduce noise then MTMF was used to generate abundances and infeasibility scores. An assessment of the success of each image product was then made based on field observations and ground spectral information.

This is an issue for discussion since the accuracy verification of hyperspectral data is difficult due to scales of measurement, geo-registration issues and limited access to ground spectrometers. In some cases, the hyperspectral data are considered to constitute evidence for the presence of a mineral, e.g. the presence of a 2.265 μm feature for jarosite. Table 3.4 gives a qualitative assessment of the MTMF mineral abundance data, based on accuracy (in relation to field observations) and noise characteristics.

Table 3.4 Assigned quality values (0 to 9 = low to high) for MTMF mineral abundance images.

	Image end-members			Reference end-members		
Range	VNIR	SWIR	VNIR-SWIR	VNIR	SWIR	VNIR-SWIR
goethite	9	0	9	8	0	7
hematite	9	0	9	3	0	0
jarosite	7	9	9	6	7	8
schwert.	5	0	8	4	0	4

The comparison of MTMF abundance image results (Table 3.4), suggests that best results are achieved by the use of image end-members and the largest spectral range. For both goethite and jarosite, USGS spectral library end-members produced useful results. However, hematite mapping was only successful using the image end-member and both hematite and goethite were not successfully mapped using the SWIR. Schwertmannite was only partially successful using the combined VNIR-SWIR image

end-member due to the inclusion of other areas - probably as a result of the impurity of the image spectrum.

Examples of abundance results for jarosite are shown in Figure 3.29. All the images are similar and have successfully mapped known jarosite zones associated with seepages on the south tailings dump (A), active weathering of pyritic rocks (B) and the fracture zone / north adit spring zone (C). The VNIR image end-member (Figure 3.29a) has included some other rocky areas generally rich in Fe-oxides (south of C) due to this part of the spectrum containing only broad features for jarosite. The laboratory jarosite end-member approach (Figure 3.29d), although still effective, tends to show more background noise and has been influenced unduly by some of the built environment features in the town.

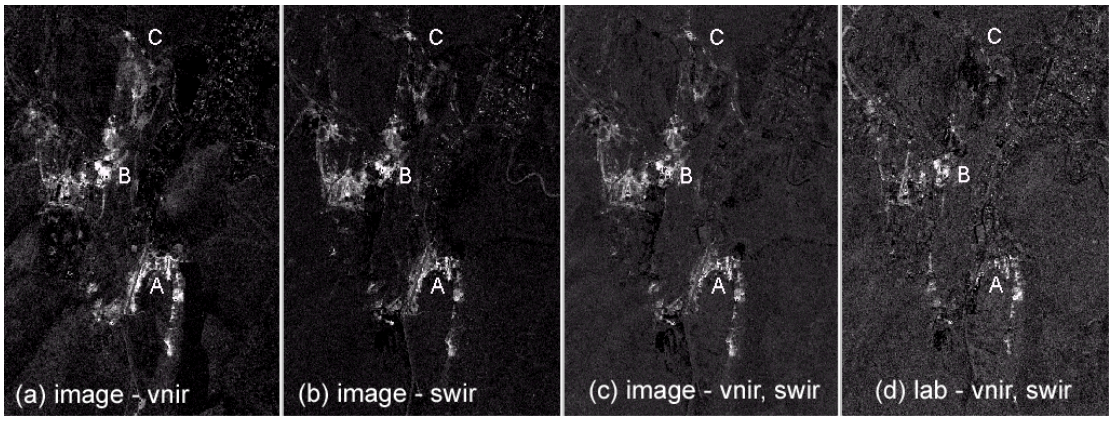

Figure 3.29. Jarosite MTMF abundance comparison. (a), (b) and (c) all use the image end-member in Figure 3.28(a) and different wavelength ranges. (d) was produced using the USGS end-member for jarosite in Figure 3.28(b).

Image end-members and the combined VNIR and SWIR spectral range were used to produce the AMD mineral map shown in Figure 3.30. High MTMF infeasibility values were masked and this removed some pixels associated with building roofs. Also for all the end-members, a threshold MTMF score of 0.30 was used to create a class map. An MTMF score of 1 indicates a perfect match between pixel spectra and target end-members and the threshold value was chosen based on ground observations. Rigorous calibration of this cut-off value was considered too exhaustive and impractical for this study. Red areas in Figure 3.30 show where schwertmannite is forming by rapid oxidation from flowing acid mine drainage (indicating pH < 4.5 – see section 3.1.3.3).

These are sources of major pollution and the largest scwertmannite zone at North Adit spring (just below C) is providing a significant flow input of pollutants to the Molonglo River. In other areas like at the north end of the south tailings dump (A in Figure 3.28), smaller seepages containing schwertmannite are found. In the middle section of the southern dump, there are a few pixels that also relate to seepages of groundwater in the dump, all contributing pollutants to the environment.

Jarosite is also formed in areas of microseepage and fracture zones. Jarosite zones on the south tailings dump, including those on the bank of the town reservoir, indicate seepage of acid groundwater interacting with weathered dump materials. These areas are also contributing toxic metals to the environment but at a slower rate than schwertmannite areas. As mentioned before, the jarosite near B is formed by weathering of pyritic mine sequence rocks and may also be contributing significant pollution during run-off periods. Goethite in some areas (green in Figure 3.30) may have been transformed from jarosite but could also be part of the weathering of volcanic rocks lacking pyrite. Hematite areas mostly represent areas where leached soils have developed. The area at D is the ore concentrate loading area and is strongly hematitic.

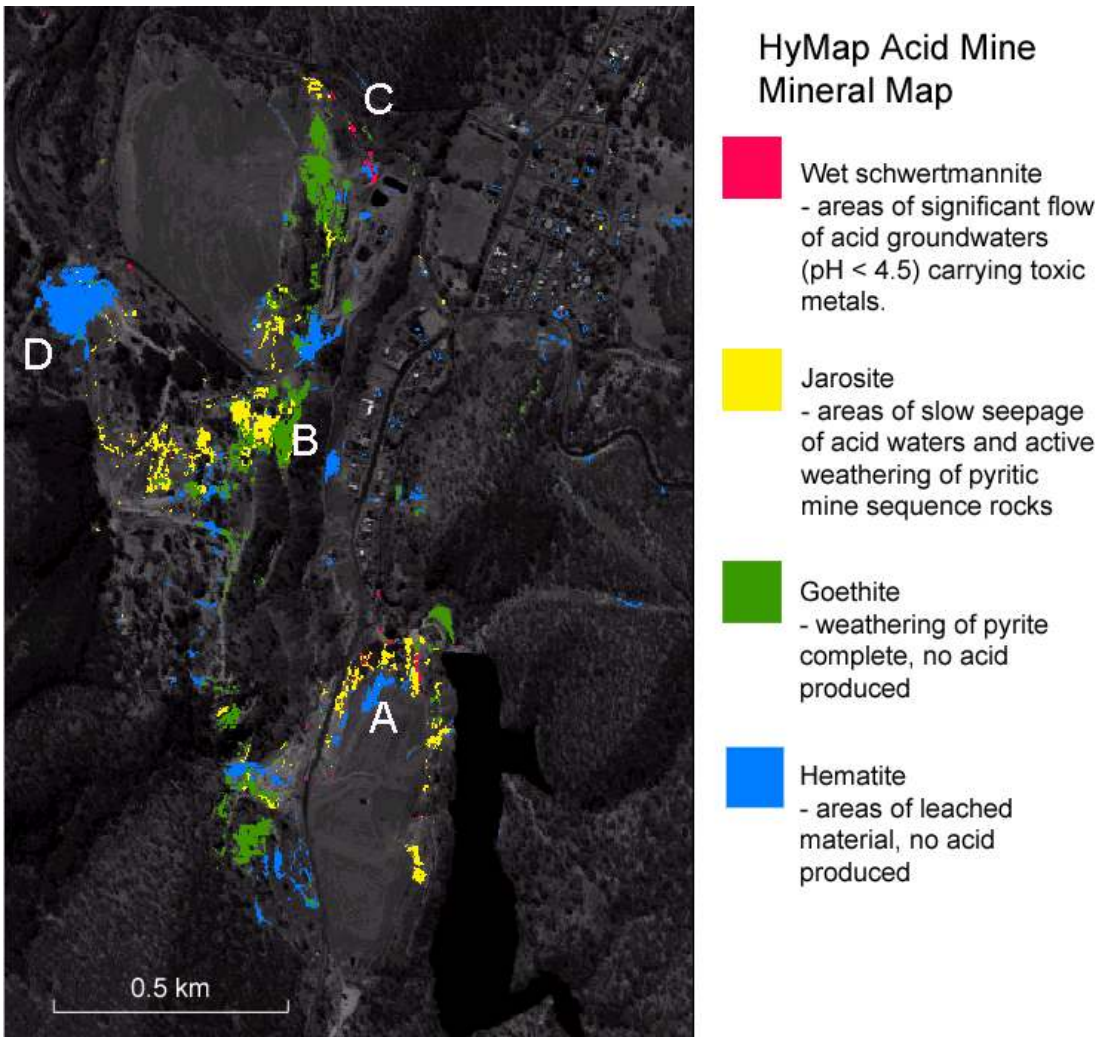

Figure 3.30. AMD mineral class map derived by unmixing of HyMap VNIR and SWIR data using image end-members.

The hyperspectral AMD mineral class map (Figure 3.30) provides a rapid mapping of continuing sources of pollution in the Captains Flat mine area. Red and yellow indicating schwertmannite and jarosite respectively show areas where acid water enters the environment. The major sources of pollution are the North Adit spring and the southern tailings dump. The proximity of these areas to the Molonglo River and town reservoir creates a major problem for rehabilitation efforts.

3.4 Conclusions

Airborne HyMap data, samples for analysis and ground spectral data were collected from the Captains Flat area with the aim of producing an airborne map of environmental hazards. Spectral data collected from AMD precipitates in the Captains Flat area show

that there is significant variability between mineral signatures. XRD, spectral studies and electron microprobe of mine drainage materials have identified schwertmannite, jarosite, goethite, gypsum and black algae. The recently discovered mineral schwertmannite is amorphous and generally present under a thin layer of water. As a result, this mixture has characteristic spectral properties. A dried schwertmannite spectrum presented here (see Figure 3.7, spectrum cf87) is one of only a few known to be measured world-wide and currently none of these have been published.

Two HyMap surveys were flown at Captains Flat because problems with the first survey, due to topographic shading, degraded the ability of the hyperspectral data to target materials. Nevertheless, the use of a shade correction (the C-correction method – see section 3.3.1.2) demonstrated an improvement in the analysis for VNIR data although the SWIR radiance was too low to achieve successful mineral mapping of jarosite. This technique was not required for the second survey but it could be useful for correcting hyperspectral data acquired elsewhere over very steep terrains.

The signatures of calibration targets deployed in the second airborne survey showed that the atmospheric correction routine “HyCorr”, incorporating ATREM, produced realistic spectra. However, application of a linear correction to the HyMap data, based on the spectra of the ground targets, revealed an artificial step in the data between the VNIR and NIR modules. This was subsequently found to have been produced from an error introduced during pre-processing, by HyVista Corporation, which was designed to correct for slight detector radiance mis-matches. Although not in time to prevent many probable “bad” batches, the company was able to repair their data product based on information from the author.

Image end-member unmixing, of atmospherically corrected HyMap data, was found to successfully identify areas of acid mine pollution at Captains Flat. HyMap-derived mineral maps for schwertmannite map the strongest flow areas of acid-mine waters while the jarosite abundance image highlights locations of acid production on weathered surfaces and at smaller seepage zones. The combined airborne mapping of these two minerals effectively shows where acid waters and toxic materials enter the environment.